# In-situ boundary layer transition detection on multi-segmental (a)synchronous morphing wings

Stuber, Vincent L.; Mkhoyan, Tigran; De Breuker, Roeland; van der Zwaag, Sybrand

**DOI**
10.1016/j.measen.2021.100356

**Publication date**
2022

**Document Version**
Final published version

**Published in**
Measurement: Sensors

Measurement: Sensors 19 (2022) 100356

Contents lists available at ScienceDirect

Measurement: Sensors

journal homepage: www.sciencedirect.com/journal/measurement-sensors

# In-situ boundary layer transition detection on multi-segmental (a) synchronous morphing wings

Vincent L. Stuber *, Tigran Mkhoyan, Roeland De Breuker, Sybrand van der Zwaag

*Delft University of Technology, Kluyverweg 1, 2629, HS Delft, the Netherlands*

ARTICLE INFO

*Keywords:*
Piezoelectricity
Laminar-to-turbulent transition
Wind tunnel experiments
Morphing wing

ABSTRACT

This paper presents an experimental method to detect in-situ the location of transition on a multi-segmental trailing edge camber morphing wing during synchronous and asynchronous morphing. The wing consists of six independently morphing segments with two of the segments instrumented with eight embedded piezoelectric sensors distributed uniformly along the chord. Using suitable data processing, each of the sensors gives a signal that can be used to determine the state of the boundary layer (laminar, transitional, turbulent) at the location of that sensor. The results showed that synchronous morphing can substantially shift the location of transition, up to 20% of the chord length for angles of attack below 9°. Differences in the location of transition up to 5% are found between the near-root and near-tip segment. Using a dedicated data processing approach, the location of transition could be reconstructed in case of complex asynchronous morphing involving one to five segments. The results show a shift in the location of transition when morphing neighboring segments, but also show that non-neighboring segments have a minimal effect. This sensing method holds significant promise for online advanced morphing control to delay transition and thereby reducing skin friction drag.

## 1. Introduction

The aerodynamic efficiency of aircraft is defined by the lift-to-drag ratio, which is strongly influenced by the type of boundary layer the wing experiences [1–3]. A way of minimizing the drag is to make a large fraction of the flow over a wing laminar, which possesses lower skin friction drag compared to turbulent flow. This is therefore often the motivation to move the so-called laminar-to-turbulent transition front towards the trailing edge (TE) of a wing. This can be achieved by designing for a delayed transition. Typical examples are natural laminar airfoils [4,5]. In addition, there are active methods to delay transition such as jet or plasma actuators [6–8], and hybrid laminar flow [9].

Morphing wings provide another active way of moving transition, as they affect the boundary layer surrounding them upon changing shape [10–15]. Studies have shown that by using morphing wings with an active extrados structure transition can be shifted by 10%–20% of the chord length [16,17]. The idea of a so-called morphing laminar wing is to have the wing change its shape such as to push the transition as close to the TE as possible to lower the overall skin friction drag. In order for such a system to work, one of the input variables required is the location of transition itself. However, the determination of the location of transition becomes complicated when considering a three dimensional flow, i.e. a wing with a free tip, as the tip vortex can locally lower the effective angle of attack. Because of this, the location of transition along the chord becomes a function of the spanwise location with transition closer to the TE near the tip of the wing [18]. Another complication occurs when a camber morphing wing has separate segments distributed along the span (of each separate wing) which can be actuated individually. This enables synchronous morphing (i.e. each segment has the same TE deflection) and asynchronous morphing (i.e. segments can have different TE deflections). This further increases the dependence of the location of transition on the spanwise location. Such an over-actuated wing has more variables than degrees of freedom, as for instance the lift can be increased by morphing a segment near the root of the wing, near the tip of the wing, along the entire span, or using any other available segmental morphing setting. Therefore, such an over-actuated wing is thought to be able to provide a higher lift-to-drag ratio by actuating appropriate patterns of segmental deflection.

One way to obtain the location of transition is through analytical models. A commonly used model is based on Xfoil [19], which was used in other work to provide the location of transition as input parameter during wind tunnel experiments on two-dimensional flows on morphing

* Corresponding author.
*E-mail addresses:* v.l.stuber@tudelft.nl (V.L. Stuber), s.vanderzwaag-1@tudelft.nl (S. van der Zwaag).

https://doi.org/10.1016/j.measen.2021.100356
Received 2 August 2021; Received in revised form 14 October 2021; Accepted 24 October 2021
Available online 3 November 2021

wings with an active extrados structure [13,16,20]. Unfortunately, the complications discussed above (three dimensional flow and asynchronous multi-segmental morphing) will make such models less accurate and wing-specific. Another way is to use sensor systems capable of detecting the location of transition. Typically such sensor systems rely on pressure or sound transducers [21–23], hot film sensors [24–28], IR thermography [29–31], or shear stress measurements [32–35]. Unfortunately, measurement techniques like these are either restricted to wind tunnel environments or require a high number of sensors to meet the required spatial resolution.

In recent work we have shown the use of piezoelectric bimorph sensors installed underneath the airfoil skin with small vanes piercing through the skin to detect vibrations in the boundary layer [36]. While such a vane causes a small turbulent wedge, it was shown that the created turbulent wedge downstream of the sensor does not influence the ability of the sensor to infer the state of the boundary layer upstream of the senor. Similar to pressure or sound transducers, such sensors are able to locally distinguish between laminar, turbulent and separated flow, and show a clear amplitude peak at transition. Such sensors still suffer from the fact that the spatial resolution is limited to the number of sensors installed, but this can mathematically be overcome by using the output of these sensors as a state variable. This can be done because, for a given free stream velocity and angle of attack, the value of their average amplitude over a well selected frequency domain is proven to be linked to the local boundary layer state. By installing multiple non-interacting sensors in a wing and recording their average amplitude for a range of angles of attack and morphing deflections, a database can be built containing typical state variable values of all sensors which can be related to the location of transition. It should be noted that the recorded state variable values strongly depend on the shape and dimensions of the wing and Reynolds number, and therefore should be recorded again if one wishes to apply it to another wing or conditions it with another (significantly different) Reynolds number. The state variable values obtained during any new measurement can then be compared to the ones stored in the database. Using a minimization algorithm, unique combinations of the angle of attack and morphing deflection can be determined, which in turn relate to the location of transition. As the found angle of attack and morphing deflection can be regarded as the effective angle of attack and morphing deflection of the morphing wing segment, this method can also be applied to cases where asynchronous morphing is applied. In that case, the imposed angle of attack and morphing deflection possibly do not match the physical angle of attack and morphing deflection found in the database, because morphing neighboring segments can effectively change the boundary layer on the instrumented segment. Therefore, using this method, this difference can be quantified, and the location of transition can be detected on a complex asynchronous morphing wing with only a limited number of sensors.

In this work, sixteen piezoelectric sensors, identical to the ones shown in earlier work [36], are installed in a NACA 6510 TE camber morphing wing containing six morphing segments along the span. Due to an elastomeric interface in between the individual morphing segments, the wing has a seamless continuous TE even while actuating each segment independently [37,38]. The wing is tested in a wind tunnel of the Delft University of Technology (TUD). Eight sensors are installed in direction of the chord in the second and the fifth morphing segment of the wing. First, measurements during synchronous morphing are performed, morphing all the segments equally. The angle of attack and synchronous TE morphing deflection are varied from $-5^\circ$ to $13^\circ$ and $-15$ mm to $+15$ mm, respectively. Using these measurements, the database is built to identify the unique amplitude of each sensor per angle of attack and morphing deflection. This database is then used to investigate asynchronous morphing cases to detect how morphing one or more neighboring segments affects the local transition on the instrumented segment. This will grant us unique insight into shifts in the location of transition on multi-segmental morphing wings during asynchronous morphing. With a future speed-up of the data acquisition and processing protocols such sensors might be used for in-situ control loops to dynamically optimize the wing shape in real-time.

To our knowledge, the deployment of such a sensory system on such a complex multi-segmental TE morphing wing has not been done before. Insights into the potential use of such a system and insight into the detection of the location of transition on morphing wings with spanwise distributed morphing will therefore act as the main contributions of the present work to the field.

## 2. Experimental setup

This section will discuss the hardware setup, the procedure used to interpret the piezoelectric sensor signals, the method used to work with the created database of sensor amplitudes, and the experimental program.

### 2.1. Hardware setup

The wind tunnel experiments were performed in the Open Jet Facility (OJF) in the High Speed Laboratory at the Delft University of Technology (TUD). The OJF has a tunnel outlet of $2.85 \times 2.85$ m and can provide an airspeed up to 35 m $s^{-1}$. The wind tunnel features a rotation table which enables remote control over the angle of attack.

The morphing wing was developed at the TUD, called the SmartX wing. Under zero morphing conditions, the wing has a NACA 6510 profile with a chord length of 0.5 m and a span of 1.8 m. The morphing concept used in the SmartX wing is based on the Translation Induced Camber (TRIC) concept that was also developed at the TUD [39]. The cross section of the wing showing this concept is shown in Fig. 1. It uses a sliding interface where the skin can be retracted or extended in order to deflect the trailing edge down or up, respectively, using an actuator positioned in the wing box. The skin is made from glass fiber reinforced epoxy with a tapered thickness, which provides the desired balance between material stiffness and compliance in order to obtain seamless chordwise morphing. The wing is divided into six segments of an equal width of 0.3 m, each capable of morphing individually. In order to obtain a continuous TE under all morphing conditions, a silicone rubber interface connects two adjacent morphing segments. Each segment is capable of deflecting the tip of the TE, $\delta$, from $-15$ mm to $+15$ mm from its neutral position, with positive deflections increasing camber, i.e. deflecting down [38]. This corresponds to a deflection angle of approximately $-10^\circ$ and $+10^\circ$ with reference to the unmorphed case with a typically defined hinge point. It should be noted that these deflections were measured without any aerodynamic load applied, and therefore, actual inflight deflections may differ. However, in this work the exact values of $\delta$ are not relevant, and we therefore simply use the values measured without any aerodynamic load. For a complete overview of the SmartX wing, see the SmartX overview paper [37].

In order to measure transition on the suction side of the wing, two

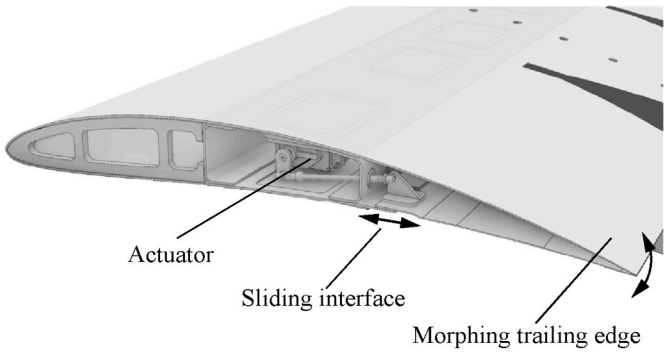


**Fig. 1.** Trailing edge camber morphing concept of the SmartX wing [37,40].

rows of eight piezoelectric sensors are installed. Fig. 2 provides an overview picture of the wing in the wind tunnel, with the dots signifying the two rows of eight piezoelectric sensors (note that not all eight are visible due to the curvature of the wing). The first set of eight sensors were installed in the second segment near the root of the wing, as is shown in the schematic given in Fig. 3. They were spaced 55 mm apart in direction of the chord and 20 mm apart in direction of the span, resulting in an angle of about 20° behind one another. Such an angle is sufficient to make sure the turbulent wedges generated by a sensor to not influence the measurement by another sensor downstream. This was confirmed using IR thermography, shown in Fig. 4. Here, the cold regions (i.e. purple regions) behind the sensors mark the turbulent wedges, which do not overlap with any of the sensors downstream. The second set of eight sensors were installed in the fifth segment near the tip of the wing, using the same spacing in a mirrored manner.

The sensors used in this work are identical to the ones used in previous work [36]. In this earlier work, Particle Image Velocimetry (PIV) measurements proved that such sensors are able to measure the state of the boundary layer, such as the transitional regime, over a classical rigid NACA 0012 airfoil. The sensors rely on the direct piezoelectric effect, i.e. generating a charge upon an applied mechanical force. They consist of piezoelectric bimorphs clamped in a 3D printed (Ultimaker 3, Ultimaker B.V., Utrecht, The Netherlands) polylactic acid (PLA) enclosure mounted underneath the top skin of the wing. On the free end of the piezoelectric bimorph a 3D printed PLA vane was glued using cyanoacrylate adhesive. This vane was installed such to protrude through an opportune opening in the skin of the wing to mechanically couple the external flow to the piezoelectric bimorph. The vane reached a height of about 1.7 mm above the wing skin, and had a width of 6.0 mm. A schematic representation of the piezoelectric bimorph including the vane inside the enclosure is given in Fig. 5. Using a shaker, the natural frequency (first bending mode) under these boundary conditions in the direction of the flow was measured to be about 3 kHz.

An ultra-low input current CMOS amplifier was directly connected to both carbon electrodes of the piezoelectric bimorph, providing a resistive load of 100 MΩ. The amplifier copies the voltage obtained from the piezoelectric bimorph, amplifies it, and drives a data acquisition unit without signal loss due to wiring and circuit load. To minimize electrical noise, the wires between the piezoelectric bimorph and amplifier were kept as short as possible, in the range of a couple of centimeters. The amplifiers send the analogue signal to a data acquisition unit (Simcenter SCADAS Mobile, Siemens), which converts it to a digital signal, at a sampling frequency of 40,960 Hz per sensor channel. In each case all sixteen sensors measured simultaneously during a 10 s time window. The remaining data processing, including fast Fourier Transform (FFT), was performed offline.

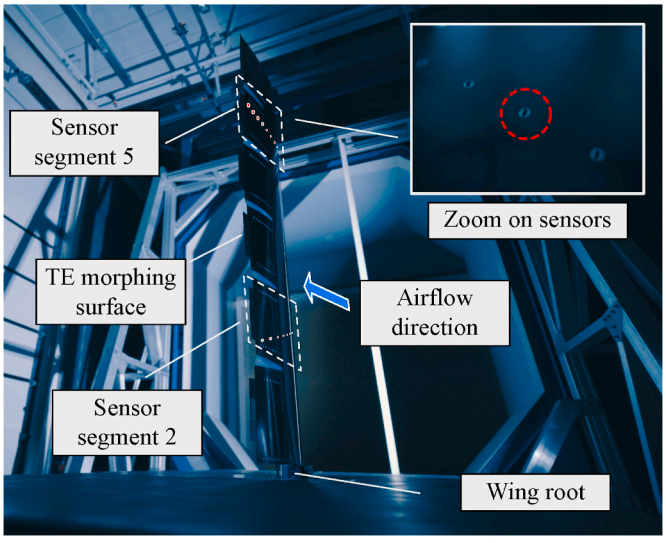


**Fig. 2.** Experimental setup in the OJF wind tunnel of the TUD. The highlighted red dots signify the locations of the visible sensors. (For interpretation of the references to colour in this figure legend, the reader is referred to the Web version of this article.)

### 2.2. Piezoelectric signal interpretation

Earlier work has shown the capability of the sensors used in this work to locate transition on a fixed NACA0012 airfoil at a chord Reynolds number of $165{\cdot}10^3$ (or an airspeed of 12.5 m $s^{-1}$) [36]. The Reynolds number used in this work is $632{\cdot}10^3$ (or an airspeed of 19.1 m $s^{-1}$), which is in the same order of magnitude, and therefore we used the same technique to find transition on the SmartX wing. In that work, it was found that frequencies above 100 Hz relate to transition. Examples of typical output signal profiles measured by a single sensor (sensor R7) at three angles of attack, are shown in Fig. 6. A clear output voltage dependence on the angle of attack is observed, which is directly caused by the state of the boundary layer exciting the sensor vane. Generally, laminar flow provides a low voltage, which in this case is at an angle of attack of 2°. At transition, vibrations in the flow tend to maximize [22]. This is measured by the piezoelectric sensors, and hence the highest voltage measured at an angle of attack of 6° signifies that transition lies closest to this sensor at this angle. The 3 kHz peak occurs due to the resonance frequency of the sensor itself. The frequencies in a turbulent boundary layer occur over a broad range of frequencies in the kHz range, causing to specifically amplify this resonance frequency. Therefore, this particular frequency has no relation to the boundary layer itself, but the magnitude of this peak does provide information about the turbulence in the boundary layer.

Fig. 7 shows the same data as is shown in Fig. 6, but now as a contour plot including all measured angles and all eight sensors installed in segment 2. In general, moving along the y-axis from low to high angle of attack, first a low intensity region is encountered. This is the regime where the boundary layer is laminar. Sensors R5 to R8 show a regime where the output voltage peaks for certain angle of attack. This is when transition has shifted to the location of the sensor. For higher values of angle of attack the local flow remains turbulent. The regions drawn into the figure act as a guide to the eye.

As mentioned before, the transition process is related to the signals measured above 100 Hz. The complex information in Fig. 7 can be simplified by integrating over the frequency from 100 Hz to 5000 Hz. The signal above the upper limit of 5000 Hz is only related to noise. The average amplitude as a function of the angle of attack for each of the eight sensors in segment 2 (indicated by R1 to R8) and segment 5 (indicated by T1 to T8) are shown in Fig. 8. We now clearly see a maximum amplitude occurring at different angles of attack for each sensor, while for some sensors that maximum does not seem to occur in range of the measured angles. From these peaks, we can deduce at what angle of attack transition occurs at which fixed position on the chord.

Comparing the location of transition measured in segment 2 and segment 5, significant differences are found. In both cases, only sensors 5 through 8 find a clear transition peak, albeit at slightly different angles. This difference is not surprising as the tip vortex plays an important role in the location of transition, and segment 5 most likely experiences this tip vortex more intensely. Comparing sensor locations to one another, it is also observed that the peaks measured near the TE (sensor R8 and T8) are relatively broad, while they become more narrow as we move towards the LE. This is an indication that the transition process becomes more abrupt as we increase the angle of attack. This makes sense as increasing the angle of attack increases the adverse pressure gradient, which in turn is a driving force to trip the flow to become turbulent.

### 2.3. The database

The obtained amplitude of each sensor, such as the ones shown in

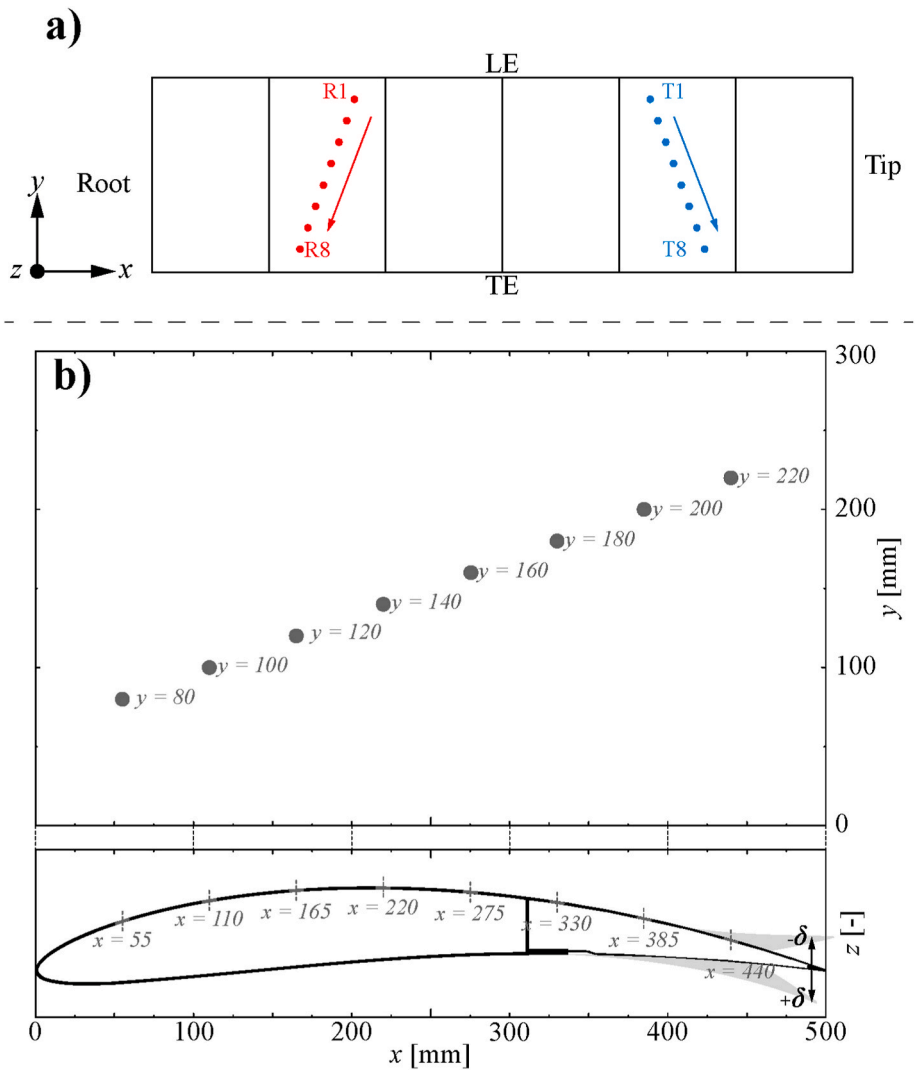


**Fig. 3.** Schematic overview of the SmartX wing. a) The piezoelectric sensors are installed in the second and the fifth segment. b) Detailed sensor positions within a single segment.

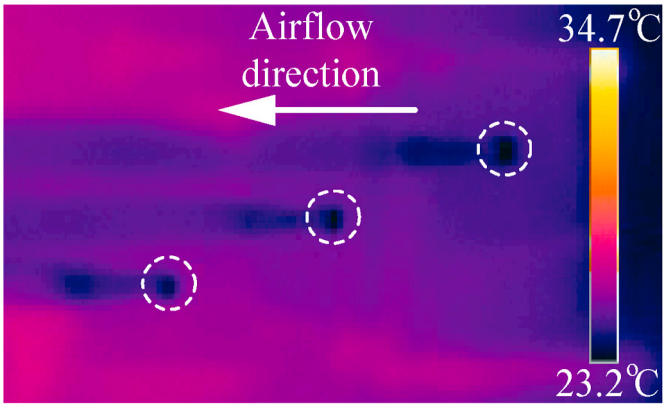


**Fig. 4.** Infrared image of the suction side of the wing, showing the turbulent wedges created by eight piezoelectric sensors while the wind tunnel operated at 19.1 m $s^{-1}$. The arrow indicates the airflow direction and the dashed circles mark sensor locations.

Fig. 8, can act as unique state variables of the boundary layer surrounding it. For instance, if we would measure an amplitude of nearly 40 mV Hz using sensor T6, we know we have to be measuring near an angle of attack of 10.5°, and we know transition has to be positioned at the location of this sensor. On the other hand, if we would measure 15 mV Hz using sensor T6, the angle of attack can still range between −5° and 8°, and hence multiple solutions can be true. However, when we consider a second sensor within the same segment, the number of possible solutions is reduced. If we consider all eight sensors within the same segments simultaneously, it is possible to extract the correct angle of attack, provided the database is properly filled. The data of Fig. 8 only considers zero morphing conditions. Upon morphing the wing, the peaks of Fig. 8 will shift to other angles and their maximum value can also change, and thus even more solutions present themselves. However, we found that when considering all eight sensors per instrumented segment simultaneously it is possible to extract both the correct angle of attack and morphing deflection. The location of transition is a function of these two values, and therefore can be extracted as well. In order to accurately do this, one would require a detailed database filled with data for many angles of attack and degrees of morphing deflection. This will therefore be the first step of the experimental program.

Once such a database is realized, it can be used to determine the change in the location of transition due to asynchronous morphing cases involving one or multiple segments in various patterns. In this case, the found values of the angle of attack and morphing deflection can be better defined as the local or fitted values, $\alpha_{fit}$ and $\delta_{fit}$, as the sensing

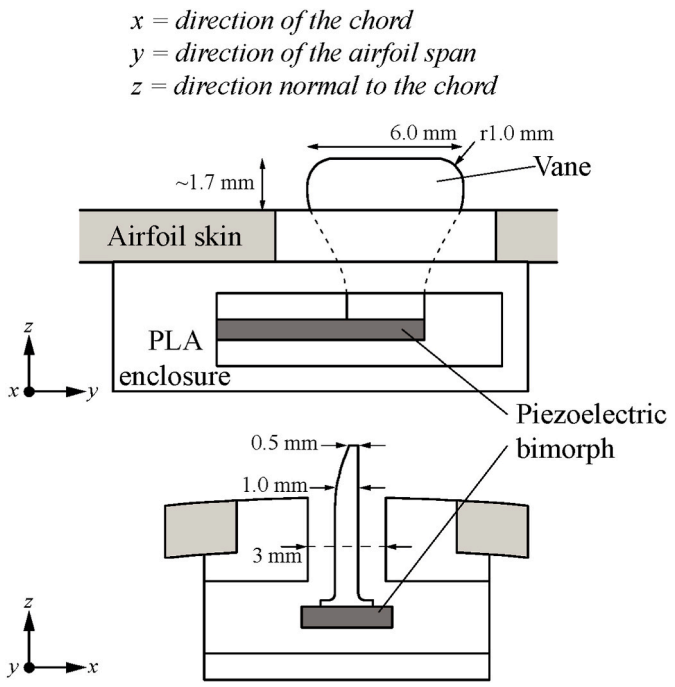


**Fig. 5.** Schematic representation of the piezoelectric bimorph inside a PLA enclosure mounted underneath the wing skin.

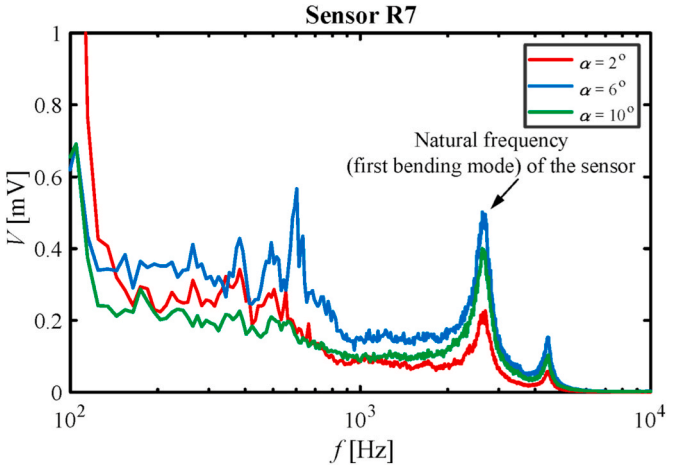


**Fig. 6.** Measured voltage, $V$, of sensor R7 versus the frequency, $f$, and angle of attack, $\alpha$, without morphing the wing ($\delta = 0$ mm).

segment likely experiences a different angle of attack and morphing deflection as the imposed ones. To obtain $\alpha_{fit}$ and $\delta_{fit}$, the following procedure is used:

1. The absolute difference of the amplitudes is calculated between the new measurement and the database. This is done per sensor and for all possible combinations of angle of attack and morphing deflection recorded in the database. So for example, the newly measured amplitude of sensor T1 is compared to all T1 amplitudes in the database. The found absolute difference, $\Delta A$, as a function of the sensor, $\alpha$ and $\delta$, can be calculated as follows:

$$\Delta A(sensor, \alpha, \delta) = |A(sensor) - A_d(sensor, \alpha, \delta)| \quad (1)$$

In here, $A$ is the amplitude of the new measurement while $A_d$ is the amplitude in the database. The output $\Delta A$ becomes a three dimensional matrix with the same dimensions as the database, being the sensor number, $\alpha$ and $\delta$.

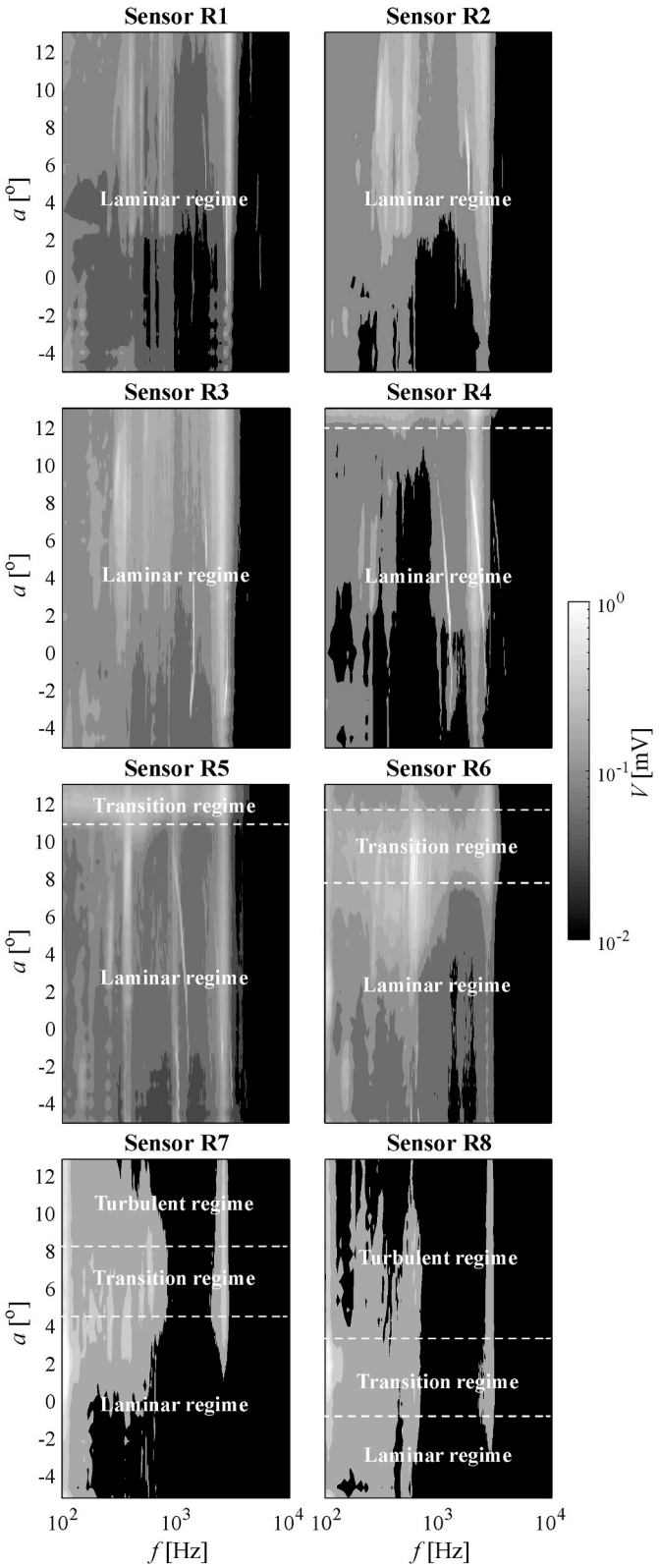


**Fig. 7.** Measured voltage, $V$, of segment 2 as a function of frequency, $f$, and angle of attack, $\alpha$, without morphing the wing ($\delta = 0$ mm).

2. The total difference per sensing segment is calculated per angle of attack and morphing deflection, adding up the $\Delta A$ of all eight sensors

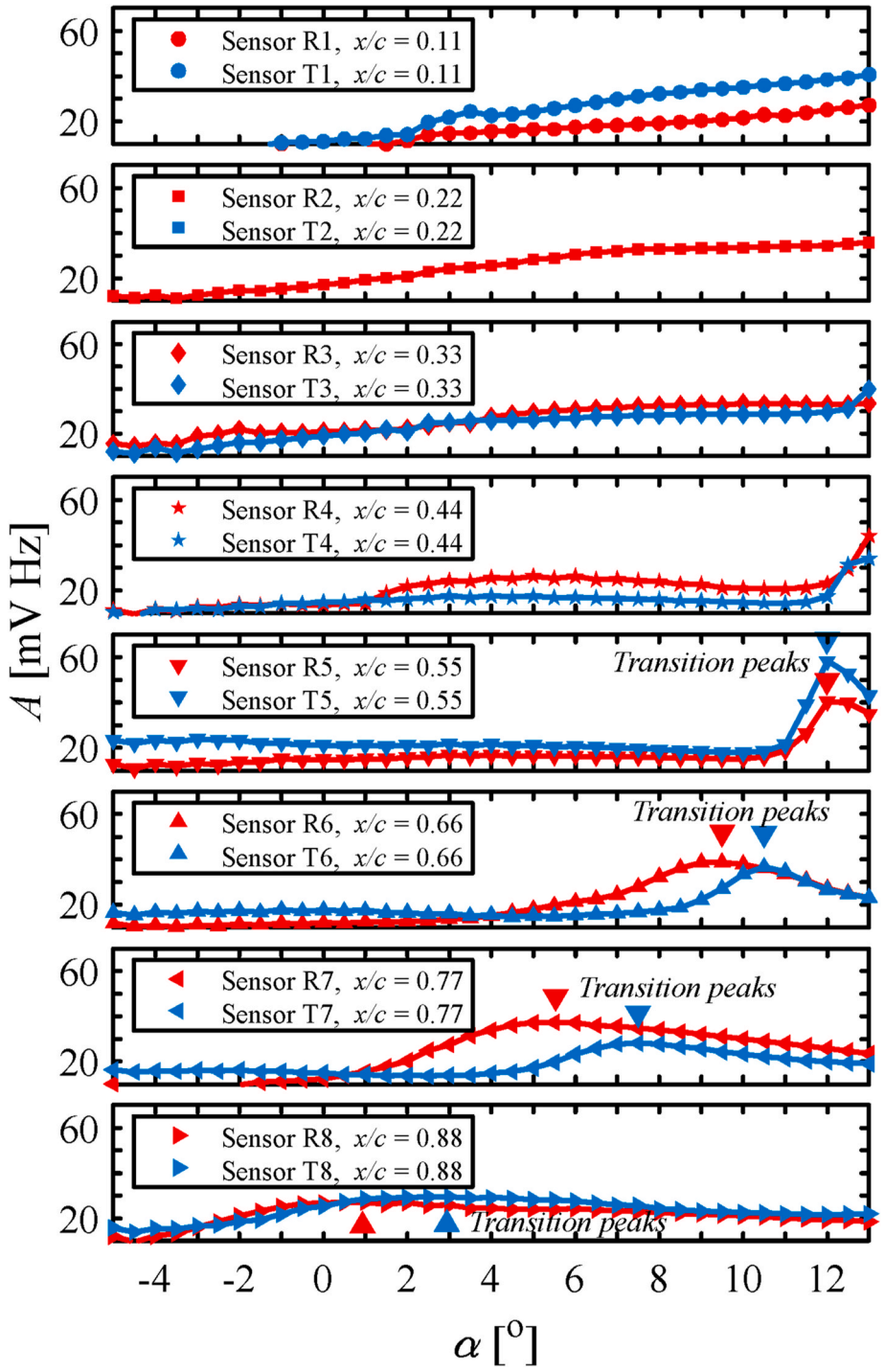


**Fig. 8.** Average amplitudes, $A$, versus the angle of attack, $\alpha$, for different sensor positions in segment 2 (R sensors) and segment 5 (T sensors), without morphing the wing ($\delta = 0$ mm).

within the same sensing segment. The found total difference, $\Delta A_{tot}$, can be calculated as follows:

$$\Delta A_{tot}(segment, \alpha, \delta) = \sum_{sensor=1}^{8} \Delta A(sensor, \alpha, \delta) \quad (2)$$

The outcome is again a three dimensional matrix, with the sensor dimension being replaced by the segment dimension.

3. The best fit is found by finding the minimum value within the $\Delta A_{tot}$ matrix. This is performed for each segment separately. The found angle of attack, $\alpha_{fit}$, and found morphing deflection, $\delta_{fit}$, are obtained as follows:

$$[\alpha_{fit}, \delta_{fit}] = \min\{\Delta A_{tot}(segment, \alpha, \delta)\} \quad (3)$$

The obtained parameters, $\alpha_{fit}$ and $\delta_{fit}$, represent the angle of attack and morphing deflection the sensing segment physically experiences.

4. During synchronous morphing $\alpha_{fit}$ and $\delta_{fit}$ should match the real and imposed values of $\alpha$ and $\delta$, as the new measurements are duplicates of the settings used to fill the database. However, during asynchronous

morphing, they most likely will not. The mismatch between them actually provides information about the effect of asynchronous morphing on the sensing segment. We can therefore define shifts in angle of attack and morphing deflection, $\alpha_{shift}$ and $\delta_{shift}$, as follows:

$$\alpha_{shift} = \alpha_{fit} - \alpha \tag{4}$$

$$\delta_{shift} = \delta_{fit} - \delta \tag{5}$$

In here, $\alpha$ and $\delta$ are the angle of attack and morphing deflection used as measurement condition, specifically of the sensing segment. It is expected that morphing a segment adjacent to the sensing segment will have a bigger impact on $\delta_{fit}$ compared to $\alpha_{fit}$. We therefore expect that $\alpha_{shift}$ will stay relatively low while $\delta_{shift}$ could show significant values.

After filling the database, a couple of synchronous morphing measurements are repeated. The database method is applied to the repeated measurements in order to find $\alpha_{fit}$ and $\delta_{fit}$. The results are shown in Table 1 $\alpha_{shift}$ and $\delta_{shift}$ appear to be zero in most cases, which was expected as the repeated cases are, just like the database recordings, synchronous morphing measurements. The minimum values of $\Delta A_{tot}$, $\min\{\Delta A_{tot}\}$, and the second minimum value of $\Delta A_{tot}$, $\min_2\{\Delta A_{tot}\}$, are presented as well. In nearly all cases a significant difference is found, meaning that it is unlikely that the incorrect minimum is taken. It should also be noted that in all cases the second minimum value occurred always in the vicinity of the minimum, meaning that it would result in a difference of only one step in $\alpha$ (= 0.5°) and/or in $\delta$ (= 5 mm).

### 2.4. Experimental program

For the experiments reported here, the wind tunnel was operating at 19.1 m $s^{-1}$, corresponding to a chord Reynolds number of $632{\cdot}10^3$. The Reynolds number was calculated using a kinematic viscosity, $\nu$, of $1.5111{\cdot}10^{-5}$ $m^2$ $s^{-1}$, and a characteristic length, $L$, of 0.5 m, equal to the chord length of the wing.

First, a complete dataset of measurements was gathered using all sixteen piezoelectric sensors installed in the wing, varying the angle of attack and synchronous morphing deflection (i.e. all six segments were given the same deflection). These measurements are used to build the database and to locate transition on the wing. During each measurement the angle of attack and morphing deflection were kept constant, while all sixteen sensors measured simultaneously during a 10 s duration. The angle of attack was varied from −5° to 13° in 0.5° increments, yielding 37 measurement points. The synchronous morphing deflection was varied from −15 mm to +15 mm in 5 mm increments, yielding 7 measurement points. All possible combinations of angle of attack and morphing deflection were structurally measured, yielding 259 measurement points in total. To ensure reproducibility and prevent system drift, the first measurement was repeated halfway through the list of measurements and once again at the end. Nearly identical results were obtained during these three measurements, with an output voltage deviation less than 2%. Only the first of these three measurements was used to fill the dataset.

Secondly, measurements were performed using asynchronous morphing (i.e. each segment was morphed individually and not all segments had the same deflection). During each measurement the angles of attack and morphing deflections were maintained for a period of 10 s while all sixteen sensors were read out. The measurements were performed at three angles of attack of 3°, 7° and 11°. Asynchronous morphing deflection patterns as reported in Table 2 were imposed. The numbers shown in the table indicate the segment numbers which were given a deflection of $\delta = -15$ mm. The adjacent segments to the actuated segments were left unactuated ($\delta$ = 0 mm), while all other segments were deflected in opposite direction ($\delta = +15$ mm). For instance, double segment setting *45* means that segments 4 and 5 have a deflection of $\delta = -15$ mm, while the adjacent segments (3 and 6) are kept at $\delta$ = 0 mm and all other segments (1 and 2) are actuated to $\delta = +15$ mm. To have the same number of segments morphing up and down per set of asynchronous settings, segment 1 and 6 were considered to be adjacent to each other.

**Table 1**
Measurements repeated after filling the database, in order to validate the database. The values in the brackets refer to $\alpha_{shift}$, $\delta_{shift}$ and $\min_2\{\Delta A_{tot}\}$.

| Repeated measurements | $\alpha_{fit}$ ($\alpha_{shift}$) [°] | $\delta_{fit}$ ($\delta_{shift}$) [mm] | $\min\{\Delta A_{tot}\}$ ($\min_2\{\Delta A_{tot}\}$) [mV Hz] |
|---|---|---|---|
| $\alpha = -5.0°$ | −4.5 | −15 | 4.19 |
| $\delta = -15$ mm | (+0.5) | (0) | (5.28) |
| $\alpha = -5.0°$ | −4.5 | +15 | 4.92 |
| $\delta = +15$ mm | (+0.5) | (0) | (8.15) |
| $\alpha = 3.0°$ | 3.0 | −15 | 2.66 |
| $\delta = -15$ mm | (0.0) | (0) | (4.63) |
| $\alpha = 3.0°$ | 2.0 | +15 | 4.09 |
| $\delta = +15$ mm | (-1.0) | (0) | (6.97) |
| $\alpha = 7.0°$ | 7.0 | −15 | 1.66 |
| $\delta = -15$ mm | (0.0) | (0) | (3.79) |
| $\alpha = 7.0°$ | 7.0 | +15 | 4.37 |
| $\delta = +15$ mm | (0.0) | (0) | (5.87) |
| $\alpha = 11.0°$ | 11.0 | −15 | 2.83 |
| $\delta = -15$ mm | (0.0) | (0) | (7.40) |
| $\alpha = 11.0°$ | 11.0 | +15 | 5.09 |
| $\delta = +15$ mm | (0.0) | (0) | (8.12) |

## 3. Results & discussion

This section will first discuss detecting transition under zero morphing conditions, then use the same detection technique while morphing the wing synchronously, and finally presents the assessment of the effects of asynchronous morphing.

### 3.1. Transition under zero morphing conditions

The location of transition of the SmartX wing under zero morphing conditions can directly be extracted from Fig. 8. The results are shown in Fig. 9 as a function of angle of attack for both segment 2 and 5. The figure also includes predicted transition positions using XFLR5, which is an airfoil analysis tool based on Xfoil [19,41]. In these calculations a NACA 6510 profile was selected with matching dimensions to the unmorphed SmartX wing, and a viscous mode Ring Vortex (VLM2) analysis was performed. To obtain the separate transition locations of segment 2 and 5, corresponding y-coordinates of 0.45 m (segment 2) and 1.35 m (segment 5) were used.

First, we address the difference between the data of segment 2 and segment 5. Both the experimental data and the XFLR5 predictions agree that transition occurs closer to the TE in segment 5 compared to segment 2. This can be explained by considering the development of the adverse pressure gradient on the suction side of the wing. The higher the adverse pressure gradient, the more they amplify instabilities in the flow and thus generate turbulence. Therefore, a higher adverse pressure gradient moves transition towards the LE. The adverse pressure gradient is not

**Table 2**
Overview of asynchronous morphing settings, where the numbers indicate the segments morphing up, while adjacent segments do not morph and all other segments are morphed down.

| Single segment settings | Double segment settings | Triple segment settings | Quadruple segment settings | Quintuple segment settings |
|---|---|---|---|---|
| 1 | 12 | 123 | 1234 | 12345 |
| 2 | 23 | 234 | 2345 | 23456 |
| 3 | 34 | 345 | 3456 | 13456 |
| 4 | 45 | 456 | 1456 | 12456 |
| 5 | 56 | 156 | 1256 | 12356 |
| 6 | 16 | 126 | 1236 | 12346 |

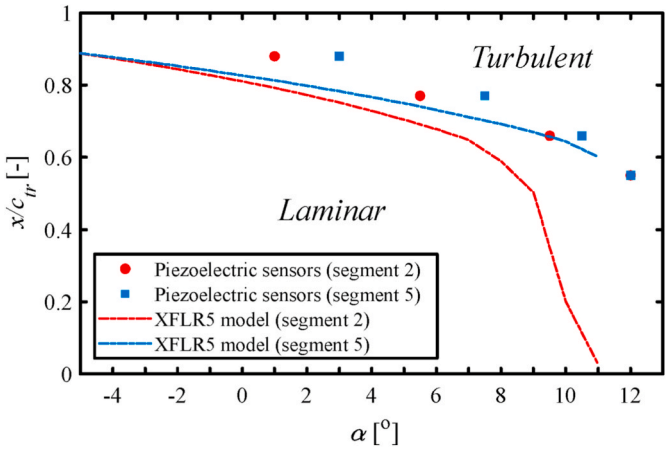


**Fig. 9.** Location of transition, $x/c_{tr}$, versus angle of attack, $\alpha$, without morphing the wing ($\delta = 0$ mm). The dash-dot lines represent the XFLR5 modelled data.

constant along the span of a finite wing. Near the tip of the wing, a strong effect of the tip vortex plays a role. Such a tip vortex occurs due to the overpressure on the pressure side of the wing to leak towards the suction side of the wing. This movement of air causes the effective angle of attack near the tip of the wing to be lower compared to the actual angle of attack [42]. A lower angle of attack generally creates a smaller adverse pressure gradient, and thus moves transition towards the TE. However, because the SmartX wing has a relatively low aspect ratio of only 3.6, the effect is likely to occur over most of the wingspan area. Still near the tip of the wing the strongest effect is expected to happen, which is why segment 5 experiences transition slightly closer to the TE.

Second, the experimental data shows transition to be closer towards the TE compared to the XFLR5 predictions. One possible explanation for this is the imperfect wing-wall interface at the root of the wing, which was there because of various cables coming out of the wing preventing us to realize a perfect walled interface. This can cause a (small) tip vortex to occur on the side of the root as well, lowering the effective angle of attack, which in turn pushes transition downstream. As mentioned before, because of the relatively small aspect ratio of the wing, this can affect both segment 2 and 5. Another reason for the difference between experimental data and the XLFR5 model could be that the SmartX wing does not resemble a perfect NACA 6510 profile due to a possible slight offset of the camber morphing TE under zero morphing conditions.

In short, the figure shows that while the absolute values do not agree between the experimental measurements and numerical model, the trends are the same. The differences can easily occur due to the imperfect wing-wall interface and a possible slight offset from a perfect NACA 6510 profile.

### 3.2. Transition shifting during synchronous morphing

Using the procedure explained in the previous section, the location of transition as a function of angle of attack and the degree of morphing deflection (using seven deflection levels) for synchronous morphing (i.e. all segments are deflected equally) was determined. As described in the experimental section, the TE camber morphing part of the wing extends up to about 20% of the chord length. The results are shown in Fig. 10, for the measurements performed on segment 2 (Fig. 10a) and segment 5 (Fig. 10b). The lines connecting the data points are constructed by edge smoothening the lines between the data points.

From the figure it can be seen that a significant shift in the location of transition can be achieved by morphing the wing (up to about 20%). Both figures show the same general trend: increasing the morphing deflection (i.e. increasing lift) moves transition downstream towards the TE, up to an angle of attack of about 11°. This trend can again be

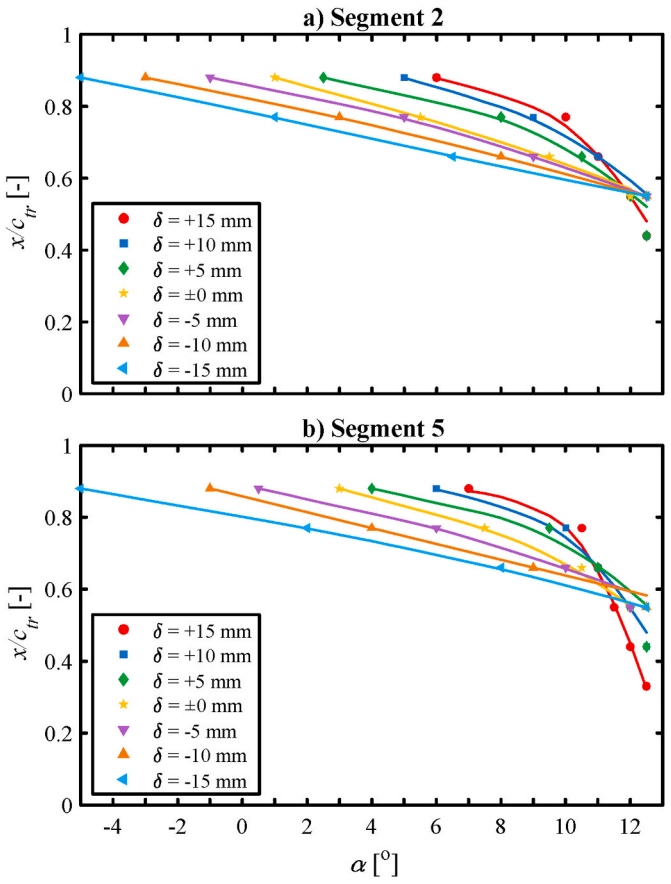


**Fig. 10.** Location of transition, $x/c_{tr}$, versus the angle of attack, $\alpha$, and synchronous morphing setting, $\delta$, given for the sensors located in a) segment 2 and b) segment 5.

explained considering the development of the adverse pressure gradient, with two counteractive factors influencing it. First, by increasing $\alpha$ and/or $\delta$, lift is increased, and directly with it, the adverse pressure gradient increases. This in turn will move transition upstream towards the LE. Second, while the increase of $\alpha$ and/or $\delta$ increases lift, so does the magnitude of the tip vortex. As described before, this inversely influences the adverse pressure gradient by lowering the effective angle of attack, and thus moves transition downstream towards the TE. One major difference between increasing $\alpha$ and $\delta$ is the development of the pressure distribution over the chord length. By increasing $\alpha$ the pressure distribution is affected over the whole chord length, while by increasing $\delta$ it mostly affects the pressure distribution in the vicinity of the morphing portion of the chord, which in case of the SmartX wing is about the last 20% of the chord. This means that the direct change of the adverse pressure gradient is more strongly affected by changing $\alpha$ in comparison to changing $\delta$. In the end it seems from the figure that in most cases for a change in $\alpha$ the direct effect on the adverse pressure gradient is dominant, while by changing $\delta$ the inverse effect, due to the tip vortex, is dominant. Only at angles of attack higher than about 11° the trends get reversed.

All sensor amplitudes used to construct Fig. 10 are transferred to the database. This database then contains the amplitudes of all sensors at all combinations of $\alpha$ and $\delta$ and contains 4144 entries; 16 (number of sensors) by 7 (number of morphing deflections) by 37 (number of angles of attack).

### 3.3. Transition during asynchronous spanwise morphing

The obtained values of $\alpha_{shift}$ and $\delta_{shift}$ for all asynchronous morphing

cases are shown in Fig. 11. They show the difference between the actual imposed values of $\alpha$ and $\delta$ of the instrumented segment, and the $\alpha_{fit}$ and $\delta_{fit}$ found as closest match in the database. The number at the x-axis presents the asynchronous morphing conditions as specified in Table 2. The numbers shown are the segment numbers which are morphed up ($\delta = -15$ mm), while adjacent segments are not morphed ($\delta = 0$ mm) and all other segments are morphed down ($\delta = +15$ mm). Segment 1 is the segment at the root while segment 6 is the segment at the tip, and these two segments are considered to be adjacent to each other.

In almost all cases, $\alpha_{shift}$ stays within 1°. This shows the accuracy of the fingerprint of the sensor amplitudes, which most strongly relate the angle of attack. As expected, the value of $\delta_{shift}$ extends to relatively large numbers, generally having an offset of about 5–10 mm and sometimes even larger. These values basically quantify the difference between the actual asynchronous measured case and the case if all segments would have the morphing configuration of the sensing segment. This definition is easier explained considering the quintuple settings (i.e. right most settings) of Fig. 11a. The $\delta_{shift}$ of settings 12345 is small because it depicts the difference between setting 12345 and the case where all segments would have the condition of the sensing segment, i.e. all have the setting of segment 2. This is already almost the case (only segment 6 is missing), and thus the shift value is low. Here, these low values of $\alpha_{shift}$ and $\delta_{shift}$ of the quintuple measurements show the repeatability of the sensor amplitudes, since the quintuple conditions are nearly identical to the synchronous morphing cases, with only a couple of exceptions. One of these exceptions is setting 13456 measured by segment 2, depicting a large $\delta_{shift}$. Here the difference is shown between setting 13456 and the case where all segments would have the condition of segment 2. In this case, none of the segments have that condition, and thus the shift value is large.

Because of the definition of $\alpha_{shift}$ and $\delta_{shift}$, the sign shows whether the sensing segment experiences a higher or lower $\alpha$ and $\delta$ due to asynchronous morphing. For instance considering the single settings (i.e. left most settings) of segment 2, setting 2 shows a large positive $\delta_{shift}$. Using this setting, the sensing segment (i.e. segment 2) has deflection $\delta = -15$ mm. The large positive $\delta_{shift}$ signifies that it actually experiences something closer to $\delta + \delta_{shift} = -5$ mm, which makes sense since the adjacent segments are both positioned at $\delta = 0$ mm. On the other hand, at setting 4 the sensing segment is at $\delta = +15$ mm, while the $\delta_{shift}$ is negative. This happens because one of the adjacent segments to the sensing segment, segment 3, has a morphing deflection of $\delta = 0$ mm, lowering the $\delta$ experienced by segment 2. It can also be seen that $\delta_{shift}$ of setting 5 is nearly zero. This makes sense, because at setting 5 segment 1, 2 and 3 are all in the same morphing position. While not all cases show such a perfect example as the once discussed in this paragraph, in general the same trends apply.

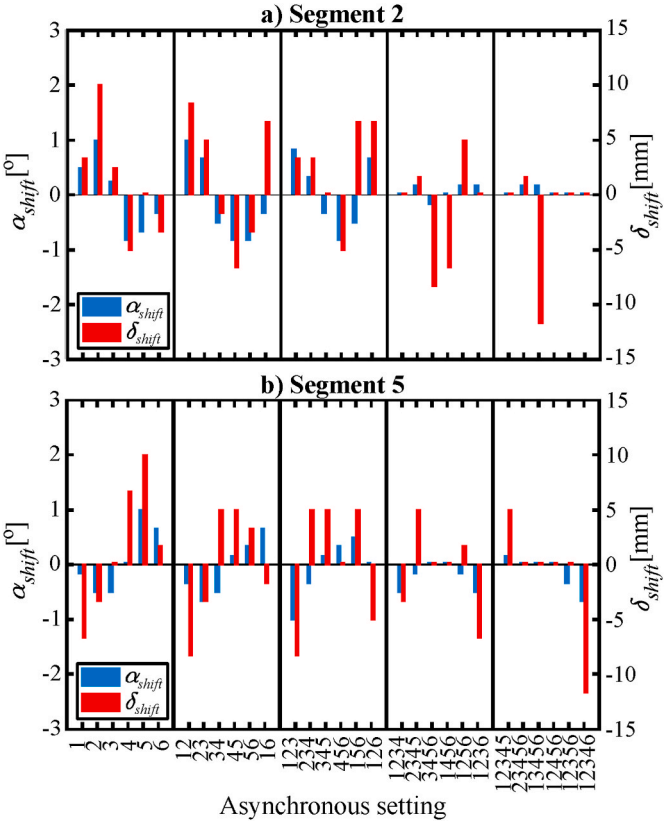


**Fig. 11.** Angle of attack and morphing deflection shift, $\alpha_{shift}$ and $\delta_{shift}$, versus asynchronous morphing setting, given for the sensors located in a) segment 2 and b) segment 5.

It is clear from Fig. 11 that in a lot of cases there is a significant shift. This means that in those cases the $\alpha$, but mainly the $\delta$, measured by the sensing segment is affected by morphing segments other than the sensing segment itself. However, this does not necessarily affect the location of transition, as a positive $\alpha_{shift}$ could counteract the effect of a positive $\delta_{shift}$.

In order to locate transition, the sensing segment is considered to be isolated, while $\alpha_{fit}$ and $\delta_{fit}$ act on it. In that case, Fig. 10 can be consulted in order to find the location of transition, using $\alpha_{fit}$ and $\delta_{fit}$. The results are shown in Fig. 12 through Fig. 16 for four different asynchronous morphing patterns. Each figure shows an example picture of the wing underneath it depicting one of the settings for clarity. The grey dashed lines are the upper and lower limits of the location of transition which are found while morphing all segments synchronously to the most upward and most downward positions (see Fig. 10).

Starting at Fig. 12a, representing the sensors in segment 2, the actual data corresponds nicely to the expected behavior. The morphing settings can be divided into three groups, being setting 2, setting 4/5/6 and setting 1/3. The first is while morphing segment 2, in which case the segment the sensors are at (also segment 2) is morphed up, causing transition to be closest to the LE. The second is while morphing segment 4, 5 or 6, in which case the segment the sensors are at is morphed down, causing transition to be closest to the TE. The third is while morphing segment 1 or 3, in which case the instrumented segment is not morphed. In this case transition lies somewhere in between. This figure (Fig. 12a) therefore actually shows that in this case there is barely any effect of the adjacent segment morphing condition on the location of transition. A similar comparison can be made using Fig. 14a, as the triple segment morphing is essentially the opposite of the single segment morphing. Here setting 456 means that those segments are morphed up, while segment 2 is morphed down, and segment 1 and 3 are not morphed. This setting therefore pushes transition closest to the TE. On the other hand setting 123, 234, and 126 (all having segment 2 morphed down) all cause transition to be equally close to the LE. Again, the other settings have a behavior in between. In a similar way the data shown in Fig. 13a, Fig. 15a and Fig. 16a can be explained, all leading to the same conclusion: the location of transition detected on segment 2 mainly depends on the morphing setting of the segment itself, and seems nearly unaffected by adjacent segment morphing.

While the data for segment 5 (the near-tip segment) at first glance looked similar to those of segment 2 (the near-root segment), closer inspection shows that there are some interesting differences. For instance in Fig. 12b it is expected that setting 4 and 6 result in similar transition locations. However, setting 4 seems to cause a transition location similar to those caused by setting 1, 2 and 3. In addition, from Fig. 14b it can be seen that setting 456 results in a different transition location compared to setting 345 or 156. In all three cases segment 5 is morphed down, but if also segments 4 and 6 morph down together with it (i.e. setting 456) the location of transition moves even closer to the LE compared to the other two settings. It seems that the adjacent segment morphing conditions for segment 5 do play a (minor) role.

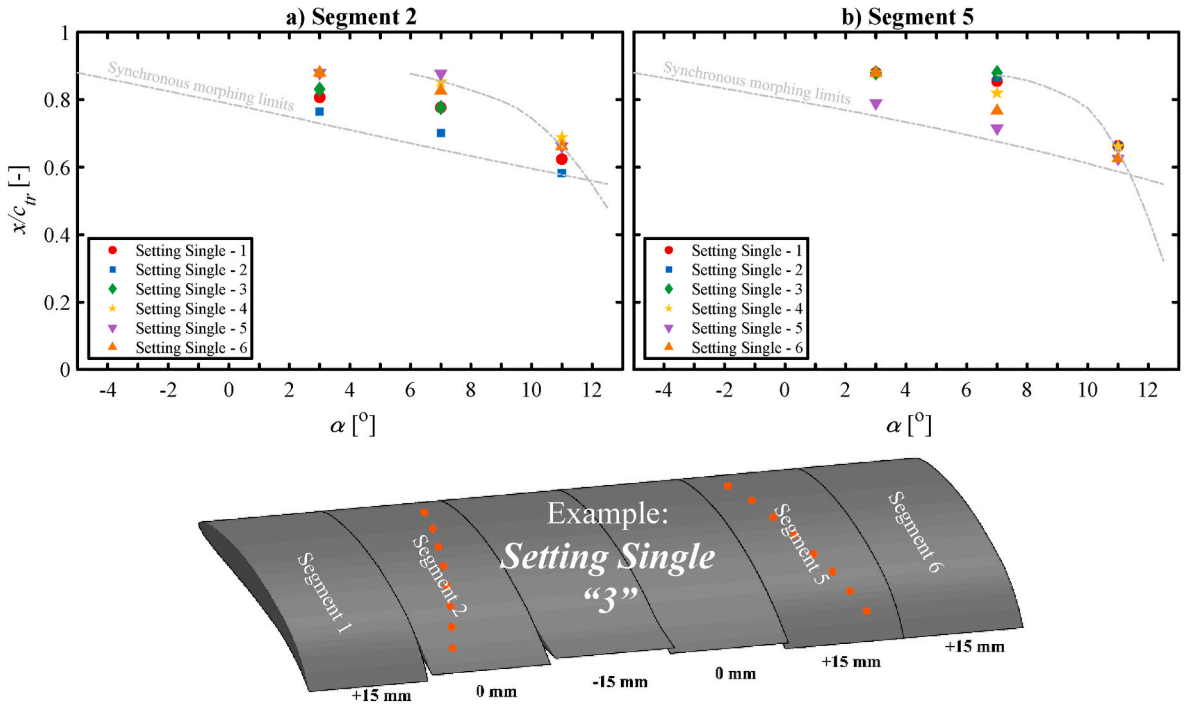


**Fig. 12.** Location of transition, $x/c_{tr}$, versus the angle of attack, $\alpha$, while morphing one segment up, given for the sensors located in a) segment 2 and b) segment 5.

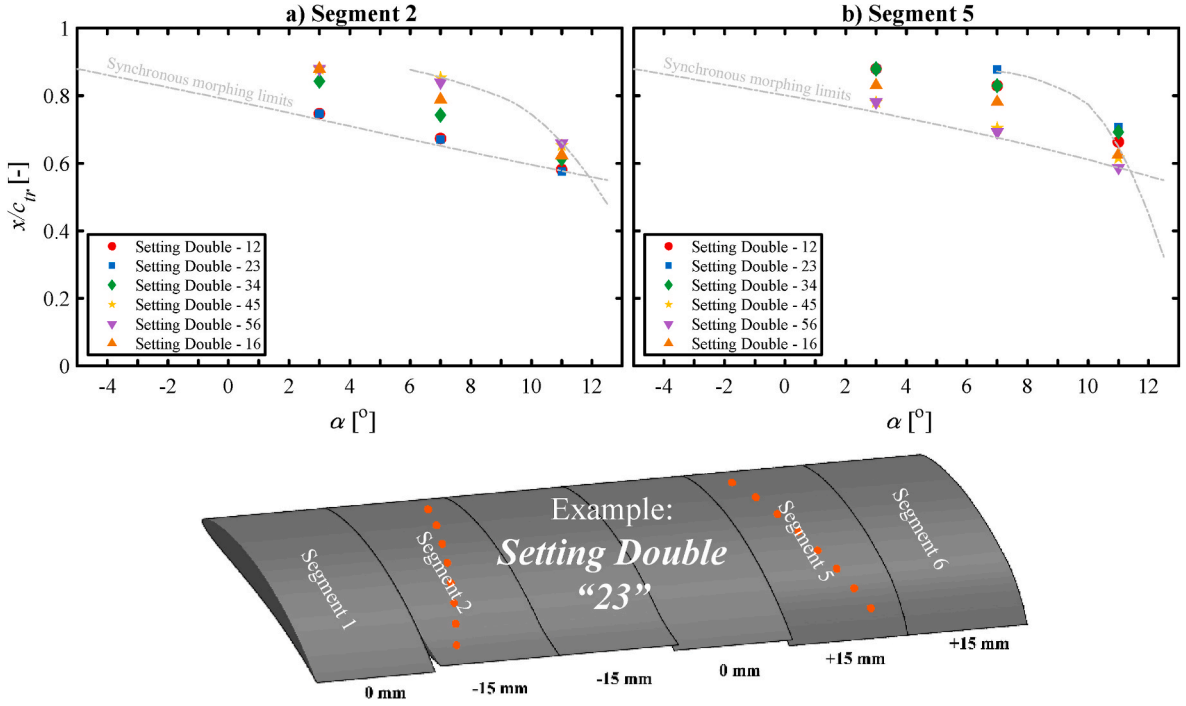


**Fig. 13.** Location of transition, $x/c_{tr}$, versus the angle of attack, $\alpha$, while morphing two segments up, given for the sensors located in a) segment 2 and b) segment 5.

One major difference between the sensors located in segment 2 and segment 5 is the magnitude of the effect that the tip vortex has on the local boundary layer. This effect is expected to be stronger near the tip, and thus stronger experienced by segment 5. We stated earlier that increasing lift due to morphing actually moves transition towards the TE (for angles of attack up to about 11°) due to the increasing strength of the tip vortex. It is to be expected that segment 6 has the highest impact on the strength of the tip vortex, and thus morphing segment 6 should result in a larger transition location shift measured by segment 5 compared to morphing the other adjacent segment (segment 4).

Considering Fig. 13b, a couple of things can be compared. First considering setting 45 and 56, where in both cases the segment 5 is morphed up together with one of the adjacent segments. If segment 6 indeed has a bigger impact on the tip vortex, setting 56 should decrease the strength of the tip vortex more and thus move transition more towards the LE. Only a small difference between settings 45 and 56 is observed, but it happens to follow the expected trend. Similarly we can compare setting 12 and 23. With setting 12 segments 45 are morphed

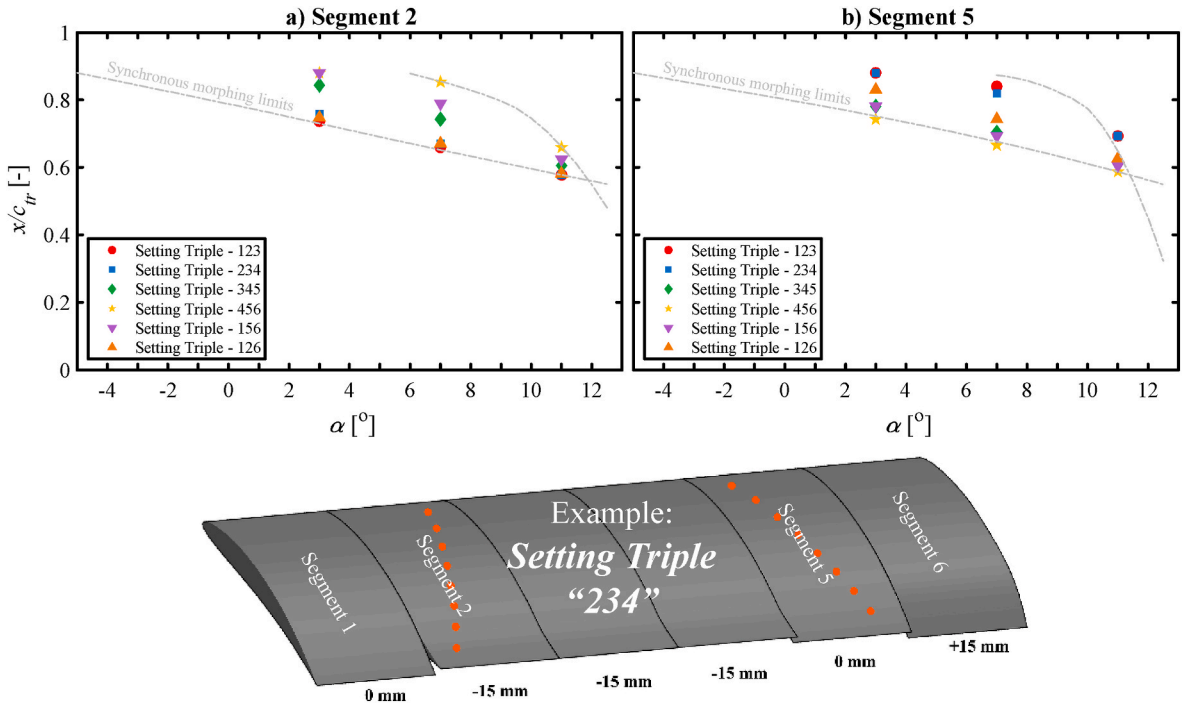


**Fig. 14.** Location of transition, $x/c_{tr}$, versus the angle of attack, $\alpha$, while morphing three segments up, given for the sensors located in a) segment 2 and b) segment 5.

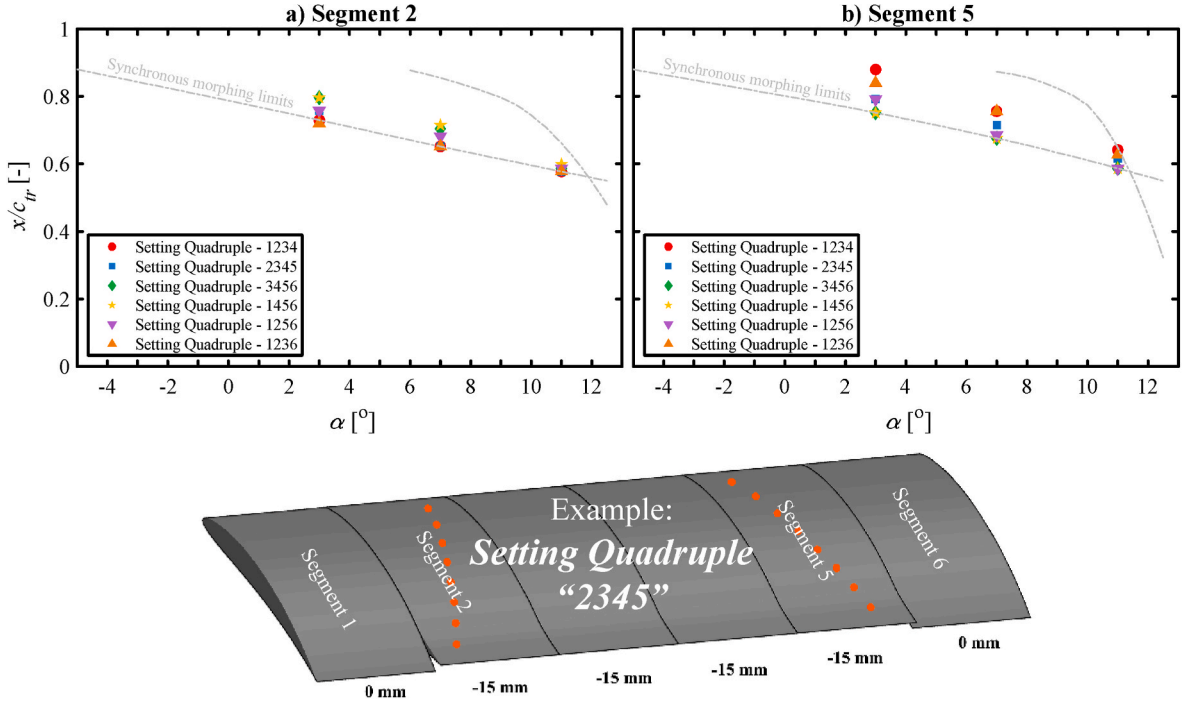


**Fig. 15.** Location of transition, $x/c_{tr}$, versus the angle of attack, $\alpha$, while morphing four segments up, given for the sensors located in a) segment 2 and b) segment 5.

down while setting 23 morphs segments 56 down. Deflecting down increases lift, and thus moves transition towards the TE. As expected, line 23 indeed lies closer to the TE compared to line 12, and thus again the expected trend is followed by the measurements.

In a similar way setting 126 and 234 from Fig. 14b can be compared. Both settings keep segment 5 at the neutral position, but setting 234 clearly causes transition to be closer to the TE compare to setting 126. This happens again because segment 6 is morphed up (setting 126) which weakens the tip vortex and moves transition towards the LE. The same is observed comparing setting 1234 and 1236 of Fig. 15b, where setting 1234 causes transition to be closer to the TE compared to setting 1236. The difference between these settings is smaller because not any of the segments reach $\delta = +15$ mm, but are kept at $\delta = 0$ mm instead. Finally, also Fig. 16b shows the same trend. Here a comparison between settings 12345 and 12356 should be made, with the transition location of setting 12345 being closer to the TE because using this setting segment 6 is kept at $\delta = 0$ mm. It is also seen that setting 12346 is even closer to the TE, meaning that the effect on the location of transition is

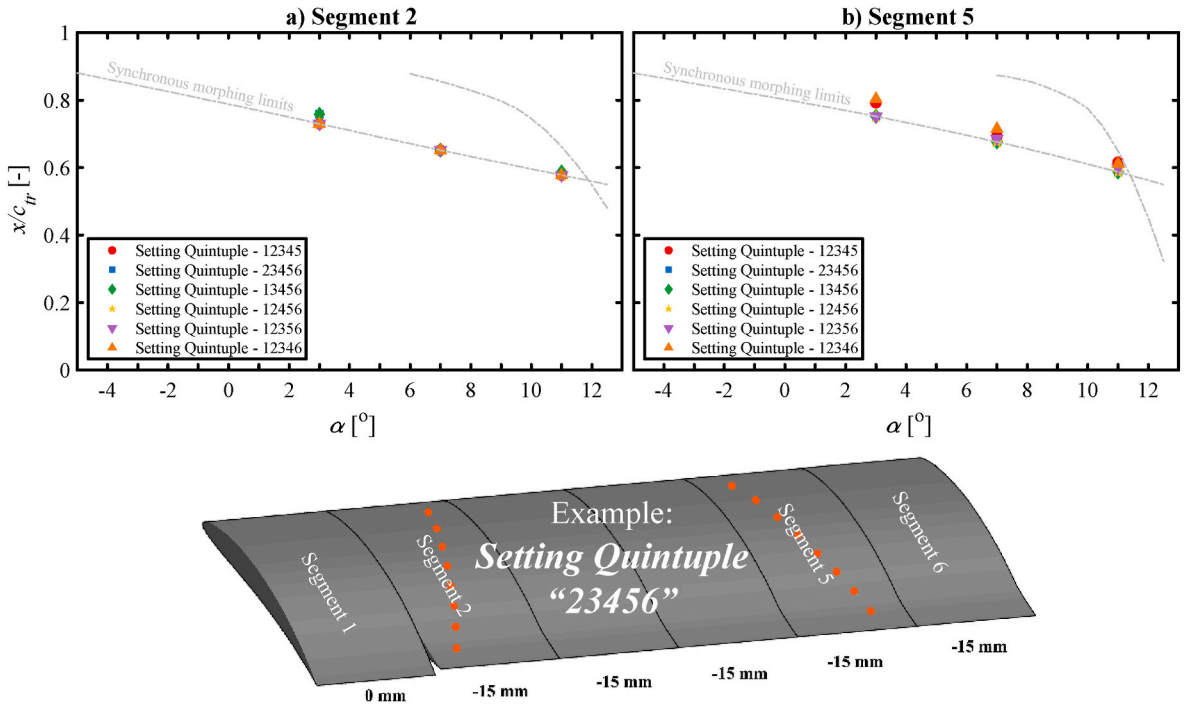


**Fig. 16.** Location of transition, $x/c_{tr}$, versus the angle of attack, $\alpha$, while morphing five segments up, given for the sensors located in a) segment 2 and b) segment 5.

still most strongly affected by morphing segment 5 itself.

Summarizing; the data shows that the location of transition in sensor segment 2 is barely affected by adjacent segment morphing. This is however not the case for sensor segment 5, positioned near to the tip of the wing. Here the tip vortex plays an important role on the location of transition. Therefore, in terms of transition location control, a morphing wing such as the SmartX wing (not swept, not tapered and multi-segmental) would benefit from having more detailed spanwise distributed morphing near the tip, while near the root of the wing a lower level of detail is sufficient.

## 4. Conclusions

A method to locate transition on a complex three dimensional multi-segmental trailing edge camber morphing wing is presented. Only sixteen sensors were installed in the top skin of the morphing wing from which the signal amplitudes are used as state variables. With these state variables measured under arbitrary conditions, it is possible to determine with a high spatial resolution the location of transition as a function of angle of attack and morphing deflection at the instrumented segment. Due to the reproducibility of the sensor amplitudes in combination with suitable data processing as described in the experimental section, we show highly consistent results, even while measuring complex asynchronous morphing conditions.

Upon morphing neighboring segments to the instrumented segment, it is found that the location of transition is barely affected near the root of the wing while a significant effect is observed near the tip. This behavior occurs due to the effect of the tip vortex, having more influence on the tip than the root of the wing. With this it can be concluded that laminar morphing wings, which are morphing wings meant to push transition towards the trailing edge for drag optimization, would benefit from having more spanwise distributed morphing segments near the tip, while a lower amount is sufficient near the root.

In the present work, the time used to measure the location of transition is set to 10 s, which was more than sufficient to obtain a strong signal-to-noise ratio. However, in order to use such a system in closed-loop control, the measurement time has to be reduced and the possibility of a sliding measurement window has to be investigated. Furthermore, parallel lift and drag measurements should be conducted to show the lift-to-drag ratio benefits such a system can provide, and a reconstruction of the location of transition along the span should be included.

## CRediT authorship contribution statement

**Vincent L. Stuber:** Conceptualization, Methodology, Software, Validation, Formal analysis, Investigation, Resources, Data curation, Writing – original draft, Writing – review & editing, Visualization. **Tigran Mkhoyan:** Conceptualization, Methodology, Software, Investigation, Resources, Writing – review & editing. **Roeland De Breuker:** Conceptualization, Methodology, Resources, Writing – review & editing, Supervision, Project administration, Funding acquisition. **Sybrand van der Zwaag:** Conceptualization, Methodology, Resources, Writing – review & editing, Supervision, Project administration, Funding acquisition.

## Declaration of competing interest

The authors declare that they have no known competing financial interests or personal relationships that could have appeared to influence the work reported in this paper.

## Acknowledgement

The authors thank Ben Schelen for his expertise and design of the electronics for the piezoelectric sensors, David Cannel for providing the required piezoelectric materials and Marios Kotsonis for his expertise on boundary layers. Furthermore, we thank Nakash Nazeer, Roger Groves and Jurij Sodja for their involvement in the development of the SmartX wing. Finally, we like to state that the original concept of the piezoelectric sensor and the SmartX wing was developed in collaboration with professor Pim Groen, who tragically passed away before the present work was concluded.

## Appendix A. Supplementary data

Supplementary data to this article can be found online at https://doi.org/10.1016/j.measen.2021.100356.

## References


[1] H. Schlichting, K. Gersten, Boundary-Layer Theory. Springer, 2017. Berlin, Germany.
[2] F.M. White, Viscous Fluid Flow, McGraw-Hill, New York, United States, 2006.
[3] M. Gad-el-Hak, "Flow control: the future,", J. Aircraft 38 (3) (2001) 402–418.
[4] Y. Zhang, X. Fang, H. Chen, S. Fu, Z. Duan, Y. Zhang, "Supercritical natural laminar flow airfoil optimization for regional aircraft wing design,", Aero. Sci. Technol. 43 (2015) 152–164.
[5] M. Fujino, Y. Yoshizaki, Y. Kawamura, "Natural-laminar-flow airfoil development for a lightweight business jet,", J. Aircraft 40 (4) (2003) 609–615.
[6] L. Cortelezzi, K.H. Lee, J. Kim, J.L. Speyer, "Skin-friction drag reduction via robust reduced-order linear feedback control,", Int. J. Comput. Fluid Dynam. 11 (1–2) (1998) 79–92.
[7] A. Abbas, et al., "Drag reduction via turbulent boundary layer flow control,", Sci. China Technol. Sci. 60 (9) (2017) 1281–1290.
[8] H.J. Tol, C.C. De Visser, M. Kotsonis, "Experimental model-based estimation and control of natural Tollmien–Schlichting waves,", AIAA J. 57 (6) (2019) 2344–2355.
[9] T.M. Young, B. Humphreys, J.P. Fielding, "Investigation of hybrid laminar flow control (HLFC) surfaces,", Aircraft Des. 4 (2–3) (2001) 127–146.
[10] S. Barbarino, O. Bilgen, R.M. Ajaj, M.I. Friswell, D.J. Inman, "A review of morphing aircraft,", J. Intell. Mater. Syst. Struct. 22 (9) (2011) 823–877.
[11] A.Y.N. Sofla, S.A. Meguid, K.T. Tan, W.K. Yeo, "Shape morphing of aircraft wing: status and challenges,", Mater. Des. 31 (3) (2010) 1284–1292.
[12] J. Sun, Q. Guan, Y. Liu, J. Leng, "Morphing aircraft based on smart materials and structures: a state-of-the-art review,", J. Intell. Mater. Syst. Struct. 27 (17) (2016) 2289–2312.
[13] T.L. Grigorie, R.M. Botez, A.V. Popov, "Self-adaptive morphing wing model, smart actuated and controlled by using a multiloop controller based on a laminar flow real time optimizer,", in: 24th AIAA/AHS Adapt. Struct. Conf., 2016 no. January.
[14] M. Arena, F. Amoroso, R. Pecora, G. Amendola, I. Dimino, A. Concilio, "Numerical and experimental validation of a full scale servo-actuated morphing aileron model,", Smart Mater. Struct. 27 (10) (2018).
[15] Y. He, S. Guo, "Modeling and experiment of a morphing wing integrated with a trailing edge control actuation system,", Chin. J. Mech. Eng. (English Ed.) 25 (2) (2012) 248–254.
[16] D. Coutu, V. Brailovski, P. Terriault, "Optimized design of an active extrados structure for an experimental morphing laminar wing,", Aero. Sci. Technol. 14 (7) (2010) 451–458.
[17] M.J.T. Kammegne, et al., "Experimental wind tunnel testing of a new multidisciplinary morphing wing model,", 18th Int. Conf. (2016) 90–97.
[18] G.E.C. Fujiwara, N.T. Nguyen, "Aeroestructural design optimization of a subsonic wing with continuous morphing trailing edge,", 35th AIAA Appl. Aerodyn. Conf (2017) no. June, 2017.
[19] M. Drela, "Implicit Implementation of the Full e$^n$ Transition Criterion,", AIAA J. Appl. Aerodyn. Conf. (2003) no. June.
[20] A. Koreanschi, O. Sugar-Gabor, R.M. Botez, "Drag optimisation of a wing equipped with a morphing upper surface,", Aeronaut. J. 120 (1225) (2016) 473–493.
[21] A.D. Gardner, K. Richter, "Boundary layer transition determination for periodic and static flows using phase-averaged pressure data,", Exp. Fluid 56 (6) (2015) 119.
[22] Ö.S. Özçakmak, N.N. Sørensen, H.A. Madsen, J.N. Sørensen, "Laminar-turbulent transition detection on airfoils by high-frequency microphone measurements,", Wind Energy 22 (10) (2019) 1356–1370.
[23] A.V. Popov, R.M. Botez, M. Labib, "Transition point detection from the surface pressure distribution for controller design,", J. Aircraft 45 (1) (2008) 23–28.
[24] A.A. Haghiri, N. Fallahpour, M. Mani, M. Tadjfar, "Experimental study of boundary layer in compressible flow using hot film sensors through statistical and qualitative methods,", J. Mech. Sci. Technol. 29 (11) (2015) 4671–4679.
[25] F. Hausmann, W. Schröder, "Coated hot-film sensors for transition detection in cruise flight,", J. Aircraft 43 (2) (2006) 456–465.
[26] H. Sturm, G. Dumstorff, P. Busche, D. Westermann, W. Lang, "Boundary layer separation and reattachment detection on airfoils by thermal flow sensors,", Sensors 12 (11) (2012) 14292–14306.
[27] B. Sun, B. Ma, P. Wang, J. Luo, J. Deng, C. Gao, "High sensitive flexible hot-film sensor for measurement of unsteady boundary layer flow,", Smart Mater. Struct. 29 (3) (2020), 35023.
[28] M. Costantini, U. Henne, S. Risius, C. Klein, "A robust method for reliable transition detection in temperature-sensitive paint data,", Aero. Sci. Technol. 113 (2021), 106702.
[29] C. Mertens, C.C. Wolf, A.D. Gardner, F.F.J. Schrijer, B.W. van Oudheusden, "Advanced infrared thermography data analysis for unsteady boundary layer transition detection,", Meas. Sci. Technol. 31 (1) (2020), 15301.
[30] C. Dollinger, M. Sorg, N. Balaresque, A. Fischer, "Measurement uncertainty of IR thermographic flow visualization measurements for transition detection on wind turbines in operation,", Exp. Therm. Fluid Sci. 97 (2018) 279–289.
[31] A.D. Gardner, C. Eder, C.C. Wolf, M. Raffel, "Analysis of differential infrared thermography for boundary layer transition detection,", Exp. Fluid 58 (9) (2017) 122.
[32] K. Liu, W. Yuan, J. Deng, B. Ma, C. Jiang, "Detecting boundary-layer separation point with a micro shear stress sensor array,", Sensors Actuators, A Phys. 139 (1–2 SPEC. ISS) (2007) 31–35.
[33] D. Roche, C. Richard, L. Eyraud, C. Audoly, "Piezoelectric bimorph bending sensor for shear-stress measurement in fluid flow,", Sensors Actuators, A Phys. 55 (no. 2–3) (1996) 157–162.
[34] B. Sun, P. Wang, J. Luo, J. Deng, S. Guo, B. Ma, "A flexible hot-film sensor array for underwater shear stress and transition measurement,", Sensors 18 (10) (2018) 3469.
[35] C. Ghouila-Houri, et al., "High temperature gradient micro-sensors array for flow separation detection and control,", Smart Mater. Struct. 28 (12) (2019), 125003.
[36] V.L. Stuber, M. Kotsonis, S. van der Zwaag, Boundary layer state detection using piezoelectric sensors, Smart Mater. Struct. (2021) accepted.
[37] R. De Breuker, et al., "Overview of the SmartX wing technology integrator,", Submitt. to AIAA J. (2021).
[38] T. Mkhoyan, N.R. Thakrar, R. De Breuker, J. Sodja, "Design and development of a seamless smart morphing wing using distributed trailing edge camber morphing for active control,", AIAA Scitech 2021 Forum (2021) no. January.
[39] N.P.M. Werter, J. Sodja, G. Spirlet, R. De Breuker, "Design and experiments of a warp induced camber and twist morphing leading and trailing edge device,", 24th AIAA/AHS Adapt. Struct. Conf. (2016) no. January.
[40] T. Mkhoyan, N.R. Thakrar, R. de Breuker, J. Sodja, "Design of a smart morphing wing using integrated and distributed trailing edge camber morphing,", ASME 2020 Conf. Smart Mater. Adapt. Struct. Intell. Syst. SMASIS 2020 (2020) no. September.
[41] A. Deperrois, "Analysis of foils and wings operating at low Reynolds numbers,", Guidel. XFLR5 (2009).
[42] J.D. Anderson, Introduction to Flight, McGraw-Hill, New York, United States, 2016.